DIGITAL ACCESS TO SCHOLARSHIP AT HARVARD
DASH.HARVARD.EDU

HARVARD LIBRARY

Flames, Splashes and Microdroplets: A Mathematical Approach to Three Fluid Dynamics Problems

Citation

Chemama, Michael Leopold. 2015. Flames, Splashes and Microdroplets: A Mathematical Approach to Three Fluid Dynamics Problems. Doctoral dissertation, Harvard University, Graduate School of Arts & Sciences.

Link

http://nrs.harvard.edu/urn-3:HUL.InstRepos:14226101

Terms of use

This article was downloaded from Harvard University's DASH repository, and is made available under the terms and conditions applicable to Other Posted Material (LAA), as set forth at
https://harvardwiki.atlassian.net/wiki/external/NGY5NDE4ZjgzNTc5NDQzMGIzZWZhMGFlOWI2M2EwYTg

Accessibility

https://accessibility.huit.harvard.edu/digital-accessibility-policy

Share Your Story

The Harvard community has made this article openly available.
Please share how this access benefits you. Submit a story

©2014 – Michael Leopold Chemama
all rights reserved.

Dissertation advisor: Professor Michael P. Brenner Michael Leopold Chemama

Flames, Splashes and Microdroplets: a Mathematical Approach to three Fluid Dynamics Problems

Abstract

Three different problems in fluid mechanics are presented in this thesis. The first one deals with the mechanism behind the extinction of a flame by an alternating electric field. A simple model for the interaction between the field and the ions produced by the reaction is presented, which agrees quantitatively with the experiments. It also indicates that charges diffusion is responsible for the non-zero time averaged force on the flame. The second problem focuses on the role of viscosity during the splash of liquid droplets. We show that contrary to what was done in previous theoretical studies, the role of viscosity cannot be investigated within the framework of a boundary layer approximation. Rather, the full viscous term must be included in the equations. Finally, we present the theory behind a new microfluidic device (called centipede) which produces microdroplets at a very high rate without relying on any active element to precipitate the detachment of the drops. We clearly show that the drops detach through a Rayleigh-Plateau instability in an otherwise quasi-static flow. We also predict how the throughput and size of the drops are affected by the geometrical parameters of the device.

Contents

0 Introduction 1

1 Extinction of flames by alternating electric fields 3
- 1.1 The experiments . . . 5
- 1.2 The model and the equations . . . 5
- 1.3 Numerical resolution . . . 10
- 1.4 Analysis of the results and scaling of the force . . . 10

2 Viscous boundary layer of splashing drops 16
- 2.1 The self-similar approach to contact . . . 18
- 2.2 The boundary layer's thickness . . . 19
- 2.3 Boundary layer's thickness and dynamical length crossover . . . 24

3 Microdroplets generation in the centipede device 27
- 3.1 The centipede device . . . 28
- 3.2 The breakup mechanism . . . 32
- 3.3 The drop's size . . . 35
- 3.4 Size limit . . . 36

Appendix A Combustion Code 38

Appendix B Surface Evolver code 43

References 54

Listing of figures

1.1 Extinction by an electric field 6
1.2 Flame in a capacitor 6
1.3 Schlieren imaging of flames 7
1.4 Ions distribution in a flame 11
1.5 Charge concentration 11
1.6 Electric field 12
1.7 Electric force 12
1.8 Charges separation 13
1.9 Measured jets' velocity 14
1.10 Computed jets' velocity 15

2.1 Sheet ejection 17
2.2 Self-similar evolution before contact 19
2.3 Dynamical length decrease 23
2.4 Viscous crossover 25
2.5 Viscous crossover phase diagram 25

3.1 Drops produced by the centipede 29
3.2 Optical micrograph of the drop makers 30
3.3 Device's parameters 31
3.4 Surface Evolver simulation 31
3.5 Drop size as a function of flux 31
3.6 Determination of the tongue radius 32
3.7 Drop precursor 33
3.8 Growth of the elliptic section 33
3.9 Critical ratio at breakup 35
3.10 Drop's diameter scaling with height 36
3.11 Maximum flux 37

To my family, who has always supported me.

Acknowledgments

I AM VERY INDEBTED to my advisor, Professor Michael Brenner, for his mentorship over the last five years. I am very fortunate that I could learn science with him because of his mastery of fluid mechanics and mathematical methods obviously, but his interests and wide knowledge encompass many other domains of science and I can only hope that some of his curiosity, enthusiasm for research and learning in general will have rubbed off on me for the future.

I am also very grateful to Professor Shreyas Mandre for all his help and the advice he gave me, not only during our collaboration on splash but also for my other projects. I had the chance to collaborate with experimentalists, and I would like to thank them for putting up with a theorist with little laboratory experience: Professors Kyle Bishop, Ludovico Cademartiri and Esther Amstad. Professor Tobias Schneider was always there when I needed help with numerical methods, sharing an office with him for two years was a great pleasure. Special thanks go to Doctor Zorana Zeravcic for all her encouragements which helped me not get discouraged when I was stuck. I would have never been able to withstand the ups and downs of research without my friends: Lihua Jin, Miriam Huntley and Doctor Beth Chen in the office, and more broadly in our group or its "extended" version: Yu Qin, Sarah Kostinski, Omer Gottesman, Joerg Fritz, John Kolinksi, Madhav Mani and Doctors Arvind Murugan, Karen Alim and Otger Campàs.

I would like to thank the following professors who agreed to be on my qualifying exams and thesis committees: Professors L. Mahadevan, James Rice, Katia Bertoldi, Vinothan Manoharan, Shmuel Rubinstein and Ariel Amir. I am grateful for their advice, suggestions and encouragements.

Finally, I would like to thank Professor Kenneth Brakke from the Department of Mathematical Sciences at Susquehanna University for his help with "Surface Evolver" while I was writing the code to simulate the flow of fluid in the microfluidics device presented in chapter 3.

0

Introduction

I completed my Ph.D. in Applied Mathematics in the group of Professor Michael P. Brenner at Harvard's School of Engineering and Applied Sciences. A physicist by training, I became more and more interested in the mathematics of modeling and decided to focus my research on problems in fluid dynamics. The fluid mechanics community at Harvard is very small and what could be seen as a negative point initially, turned out to be a very positive thing as it forced me to collaborate with people in different departments and with different backgrounds but who had a fluid mechanics problem to solve.

This is how I started to work with Doctors Ludovico Cademartiri and Kyle Bishop from the chemistry department. Our project on flame extinction is presented in chapter 1. For my second project I worked on a much more fundamental problem, drop splashing, with the help of Professor Shreyas Mandre at Brown University. My main results are summed up in chapter 2. Finally in chapter 3 is the work I did with Doctor Esther Amstad on a microfluidics device that she invented while she was a post-doc in Professor David Weitz' laboratory.

1

Extinction of flames by alternating electric fields

In 2008, the Defense Advanced Research Projects Agency (DARPA) launched the Instant Fire Suppression program to study the extinction of flames by electromagnetic fields and acoustic waves. Traditional fire-fighting techniques aim to disrupt the chemical reactions involved in combus-

tion. For example pouring water inhibits combustion by cooling flames below the critical temperature at which the reactions can happen; spraying carbon dioxide suffocates the fire by diluting the surrounding oxygen; flame retardants foams do both. These techniques are not without limitations: they are not adapted to all types of fires, they can be toxic for the environment, cause collateral damage to valuable property and they require large quantities of water, gas or chemicals to be delivered to the zone of fire. Electromagnetic fields or acoustic waves, if able to extinguish fires, would allow to avoid many of the shortcomings of the traditional methods.

It is in this context that a team led by Kyle Bishop and Ludovico Cademartiri from the Whitesides Research Group in the chemistry department at Harvard University started investigating the response of flames to electric fields, with the objective of finding ways to put them out.

The electric properties of flames were noticed already at the beginning of the 17th century. Sir William Gilbert, physician to Queen Elizabeth I and one of the early investigators of electricity and magnetism describes attempts to attract flames to electrically charged bodies.[10] Later on, experiments by scientists such as Bacon, Priestley and Volta showed that flames were conductors of electricity and could be deflected by electric fields.[23] Over the years, many more observations were made, often with contradictory interpretations and much work between 1920 and 1940 tried to answer the question of whether the electric field modified the chemical kinetics in the flame[1] or whether the force it creates on charge carriers was enough to explain experimental results.[11] Lawton and Weinberg,[17,18] among others, studied the effects of the field on the macroscopic movement of the ions and their transfers of momentum to the neutral gas. They showed that many effects could be explained by this so-called "ionic wind". However, when fields are stronger than 10^6 V/m microscopic effects cannot be ignored any more. The experiments studied here remain below this limit and so chemical effects will not be considered.

1.1 The experiments

As explained in details by Bishop and Cademartiri,[6] previous efforts to manipulate flames with electric winds have relied almost exclusively on static (dc) fields to induce steady currents of charged species that drive steady gas flows. Despite promising demonstrations (e.g., enhancing flame stability, manipulating heat transfer and reducing pollutant emissions) the magnitude of these effects, as well as their applicability, is strictly limited by ionic screening, which requires direct contact of the electrodes and the flame to maximize the ionic currents and gas velocities.[17] This led the Whitesides' laboratory team to try alternating (ac) fields. At first glance, the flame should have no net time-averaged response to such a field, however the team was able to bend and even extinguish flames. In what follows, we develop a theory of the interaction which sheds light on the mechanism for extinction by an ac field and agrees quantitatively with experimental results. The experiments are described in "ac electric fields drive steady flows in flames".[6]

1.2 The model and the equations

We propose to determine the time-averaged electric force acting on a flame between the two plates of a capacitor. The imposed electric field acts on the charges produced by the chemical reactions occurring in the flame front. For ion-doped flames, such as the ones used in our experiments the symmetry of the gas jets induced by static fields (Figure 1.3) suggests that positive and negative ions have similar mobilities; in general, this is not the case (e.g., for premixed flames with large electron densities or for sooting flames).[3] In our simple model, we will consider two effective charge carrier species, with opposite charges $\pm qe$ and equal mobility K or, equivalently, the same diffusion constants D (by the Einstein-Smoluchowski's relation:[32] $K = qeD/kT$ where k is Boltzmann's constant and T the temperature).

Let $c(\vec{x}, t)$ be the charge concentration; the imposed field $\vec{E}_0(t)$ is modified according to Maxwell-

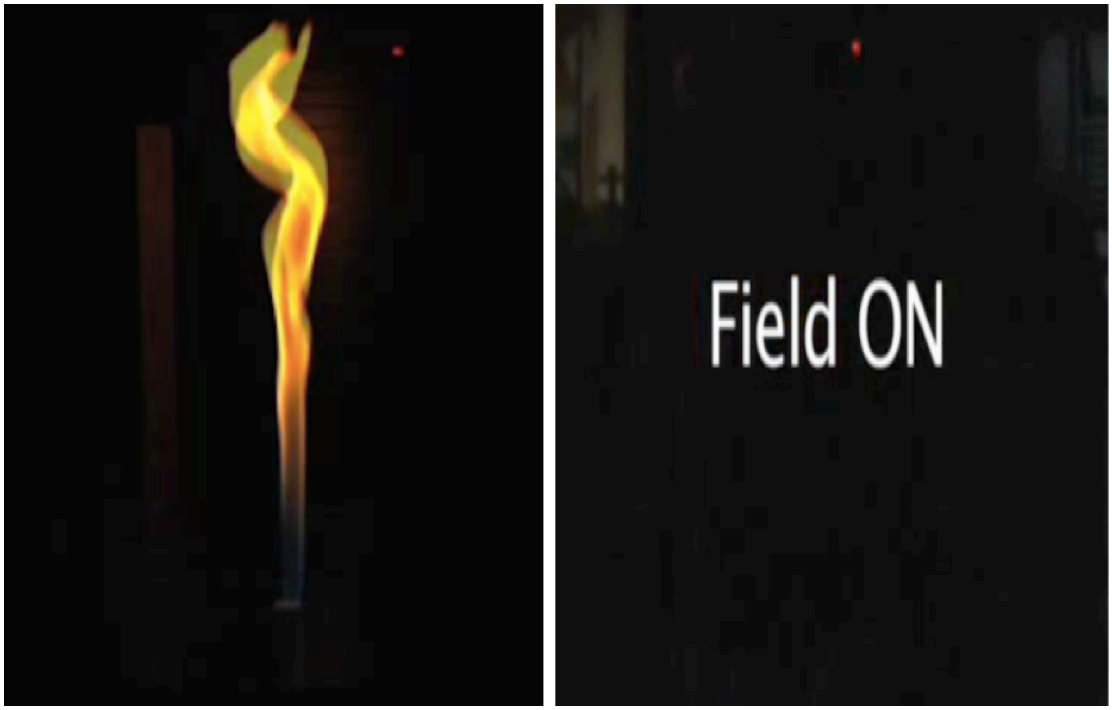

Figure 1.1: Methane flame being extinguished by the electric field created by a point electrode.

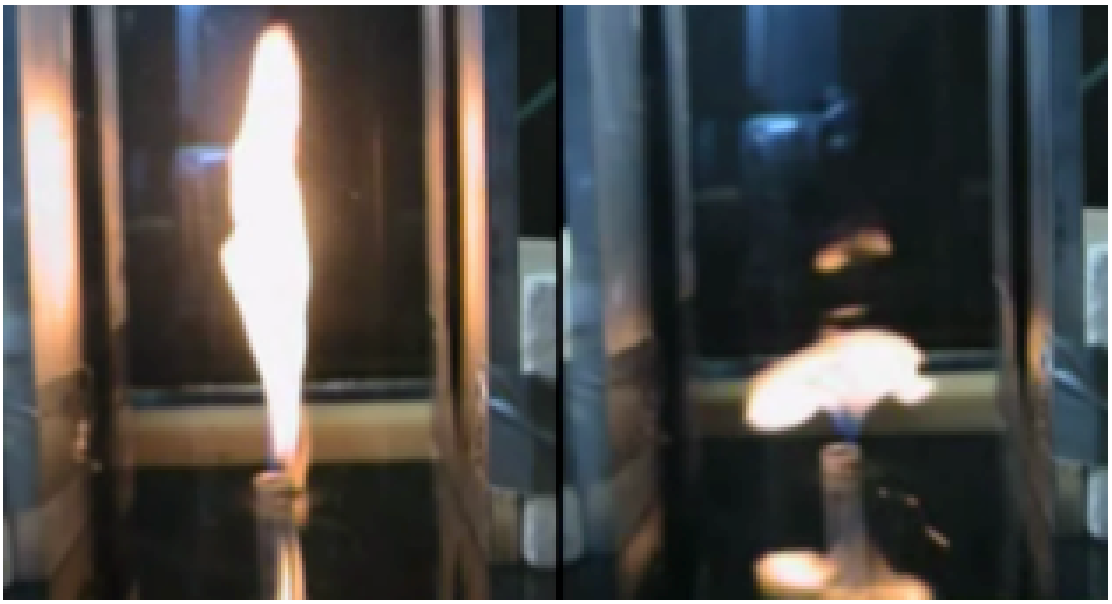

Figure 1.2: Methane flame in a capacitor with field off (left) and on (right). The force field is clearly visible.

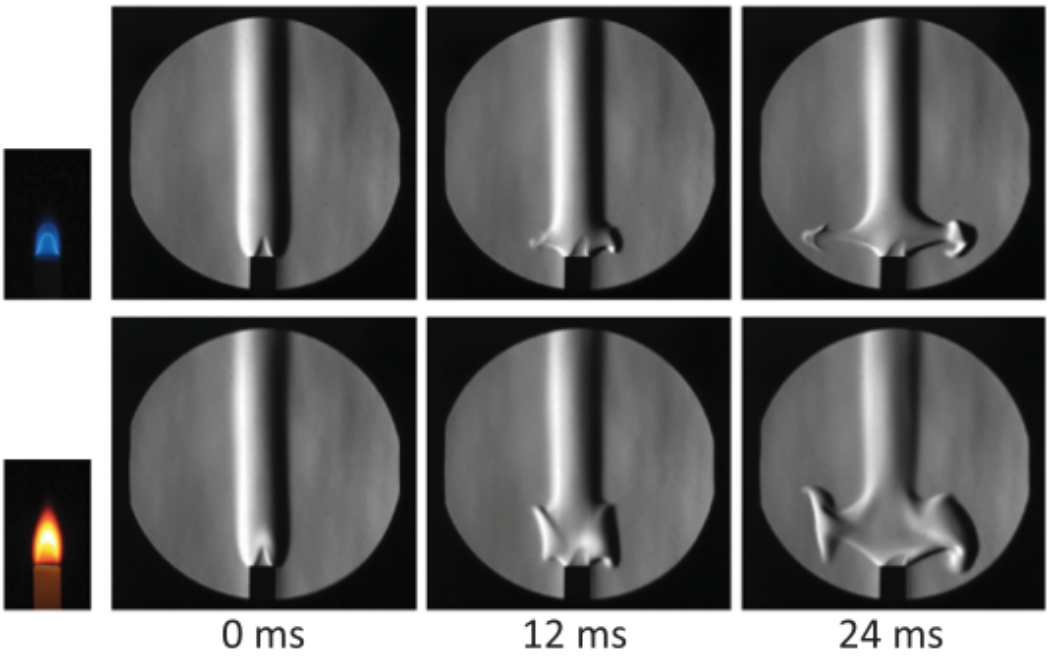

Figure 1.3: Schlieren images of a premixed methane flame without (top) and with (bottom) NaOH dopant directly after the application of a static electric field of 280 kV/m.

Gauss equation:

$$\vec{\nabla}.\vec{E}(\vec{x},t) = \frac{c(\vec{x},t)}{\varepsilon_0} \qquad \vec{E}(\vec{x},t) \to \vec{E}_0(t) \text{ as } |\vec{x}| \to L \tag{1.1}$$

Mass conservation imposes for both positive and negative charges:

$$\frac{\partial c_i}{\partial t} + \vec{\nabla}.(c_i\vec{v}_i) = \dot{c}_i \tag{1.2}$$

where $\dot{c}_i$ represents the rate of production/loss of charges i and is a function of all the other species concentrations. To maintain neutrality, we must have: $\dot{c}_+ = \dot{c}_-$. A constitutive relation is assumed that relates $\vec{v}_i$ to the mass average velocity $\vec{v}$. In the presence of an electric field $\vec{E}$ it takes the form:[33]

$$\vec{v}_i = \vec{v} - \frac{D}{c_i}\vec{\nabla}c_i + \frac{q_i eD}{kT}\vec{E} \tag{1.3}$$

For most combustion phenomena, the kinetic energy is much smaller than the thermal energy. This implies that the characteristic Mach number of the flow is small[16] and so we have $\vec{\nabla}.\vec{v} = 0$. Equation 1.2 leads to the following two equations for $c = c_+ - c_-$ and $s = c_+ + c_-$:

$$\frac{\partial c}{\partial t} + \vec{v}.\vec{\nabla}c - \vec{\nabla}.(D\vec{\nabla}c) + \vec{\nabla}.(\frac{qeD}{kT}s\vec{E}) = 0 \tag{1.4}$$

$$\frac{\partial s}{\partial t} + \vec{v}.\vec{\nabla}s - \vec{\nabla}.(D\vec{\nabla}s) + \vec{\nabla}.(\frac{qeD}{kT}c\vec{E}) = \dot{c}_+ + \dot{c}_- \tag{1.5}$$

Solving these equations requires knowing the exact expression for the rate of production of charges, and the concentration of all species. Fortunately, another relation relates c to s. Provided the time over which the electric field varies is much bigger than the time between particle collisions, the plasma in the flame is described by Maxwell-Boltzmann statistics. Let $\Phi(\vec{x},t)$ be the electric potential and $c_0(\vec{x})$

the distribution of charges when $\Phi = 0$.

$$c_+(\vec{x}, t) = c_0(\vec{x}) \exp(-\frac{qe\Phi}{kT}) \qquad c_-(\vec{x}, t) = c_0(\vec{x}) \exp(\frac{qe\Phi}{kT}) \tag{1.6}$$

Therefore c and s are given by:

$$c(\vec{x}, t) = 2c_0(\vec{x}) \sinh(-\frac{qe\Phi}{kT}) \qquad s(\vec{x}, t) = 2c_0(\vec{x}) \cosh(\frac{qe\Phi}{kT}) \tag{1.7}$$

s can be rewritten $s(\vec{x}, t) = 2c_0(\vec{x}, t)\sqrt{1 + c^2/4c_0^2}$. We assume and check later (see Figure 1.8) that charges separation is weak, and therefore $c^2/4c_0^2 << 1$. We can then approximate $s(\vec{x}, t) \sim 2c_0(\vec{x})$.

The system we have to solve in order to find the electric force $\vec{F}(\vec{x}, t) = qec(\vec{x}, t)\vec{E}(\vec{x}, t)$ is then:

$$\frac{\partial c}{\partial t} + \vec{v}.\vec{\nabla}c - \vec{\nabla}.(D\vec{\nabla}c) + \vec{\nabla}.(\frac{2qeD}{kT}c_0\vec{E}) = 0 \qquad \vec{\nabla}.\vec{E} = \frac{c}{\varepsilon_0} \tag{1.8}$$

with the following boundary conditions:

$$c(\vec{x}, t) \to 0 \text{ and } \vec{E}(\vec{x}, t) \to \vec{E}_0(t) \text{ as } |\vec{x}| \to L \tag{1.9}$$

In order to solve 1.8 and 1.9 we will make a few simplifying assumptions. The field's action on the charges is mostly along its direction, x, and so we only consider this dimension. The advection term $\vec{v}.\vec{\nabla}c$ is negligible as the velocity, driven by buoyancy is mainly vertical while the concentration gradient, driven by the field, is horizontal. The diffusion coefficient D varies with temperature; however, as explained by C.K. Law in "Combustion Physics",[16] the product ϱD is roughly constant, with ϱ the average density of the reacting gas. We therefore introduce D_0, the diffusion at room temperature T_0 knowing that $\varrho D = \varrho_0 D_0$. It can be shown[16] that pressure variations are proportional to the square of the Mach number and so we will neglect them. The equation of state is then: $p_0 = \varrho RT/\mathcal{M}$ with $\mathcal{M}$ the molar mass of air. The diffusion coefficient is given by $D = D_0 T/T_0$.

1.3 Numerical resolution

With the above approximations, we obtain the following system:

$$\frac{\partial c}{\partial t} - \frac{D_0}{T_0}\frac{\partial T}{\partial x}\frac{\partial c}{\partial x} - \frac{D_0}{T_0}T\frac{\partial^2 c}{\partial x^2} + \frac{2qeD_0}{kT_0}\frac{\partial(c_0 E)}{\partial x} = 0 \qquad \frac{\partial E}{\partial x} = \frac{c}{\varepsilon_0} \tag{1.10}$$

$$c(x,t) \to 0 \text{ and } E(x,t) \to E_0(t) \text{ as } x \to \pm L \tag{1.11}$$

The fact that the equations are invariant by translation in time leads us to look for solutions of the form $c(x,t) = Re[c(x)e^{-i\omega t}]$ and $E(x,t) = Re[E(x)e^{-i\omega t}]$. The boundary condition 1.11 must be valid for any value of L provided that it is large enough,[6] therefore ω must be the frequency of the imposed field. We solve the boundary value problem using the function bvp4c of Matlab. Of course we do not know what the functions T_0 and c_0 are exactly, however we can take a functional form that reflects our physical knowledge of a flame. We know that the typical ions density in a flame is 10^{17} ions per cubic meter, and in absence of fields their distribution has a width of order 1 cm. The temperature is maximal in the reaction zone (a few thousands K) and decreases to room temperature over a few centimeters. The literature on ions in flames is very rich, more information can be found in the article by Calcote[3] from which the figure 1.4 was taken. A very detailed reference is the paper by Fialkov.[8] The code used to solve the equations can be found in appendix A. Figures 1.5 to 1.7 show the results obtained for an imposed field with $E0 = 300\ kV.m^{-1}$ and $\omega = 1\ kHz$.

1.4 Analysis of the results and scaling of the force

The graph we obtained for the force (Figure 1.7) corresponds to what we see experimentally (Figure 1.2). The left-right symmetry is preserved and a force pulling the flame in both directions is created. Its order of magnitude, the same as that of gravity for the fields typically used, was expected for any

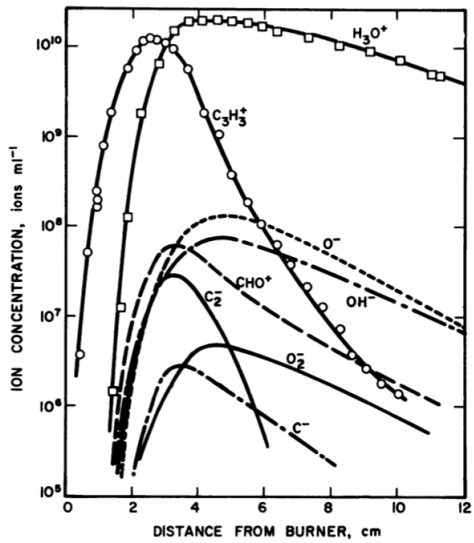

Fig. 4. Typical flame ion profiles.[32] Stoichiometric acetylene/oxygen; pressure, 1 Torr; adiabatic flame temperature, 2500°K; total flow, 70 ml sec^{-1} (STP); burner diameter, 15cm.

Figure 1.4: Figure taken from "Negative and Secondary Ion Formation in Low-Pressure Flame"[3]

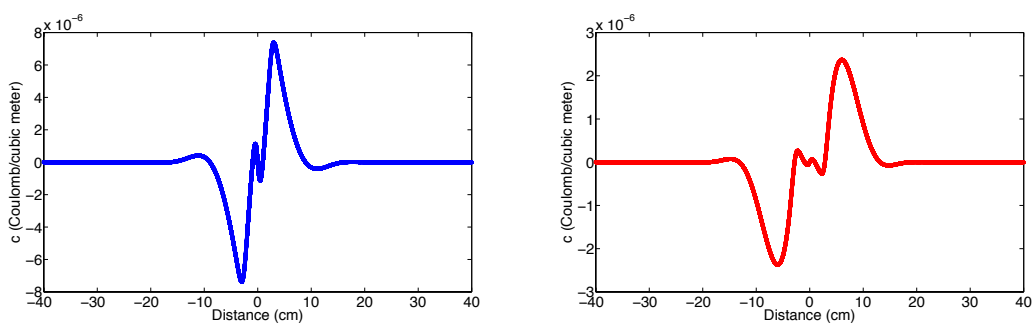

(a) The real part

(b) The imaginary part

Figure 1.5: The charge concentration as a function of the distance from the center of the flame

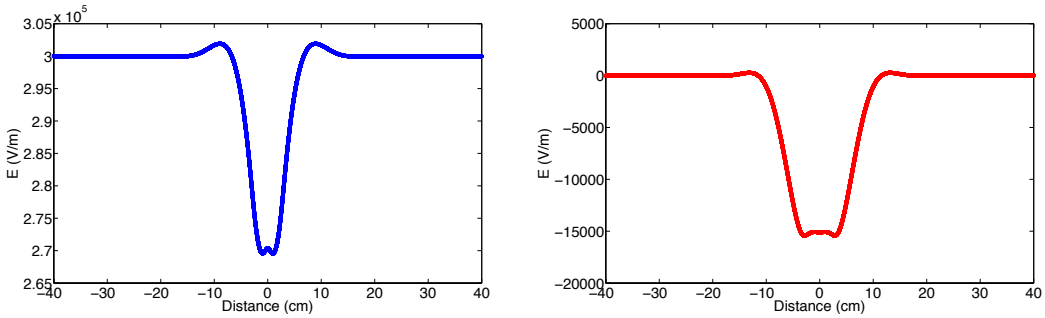

(a) The real part

(b) The imaginary part

Figure 1.6: The electric field as a function of the distance from the center of the flame

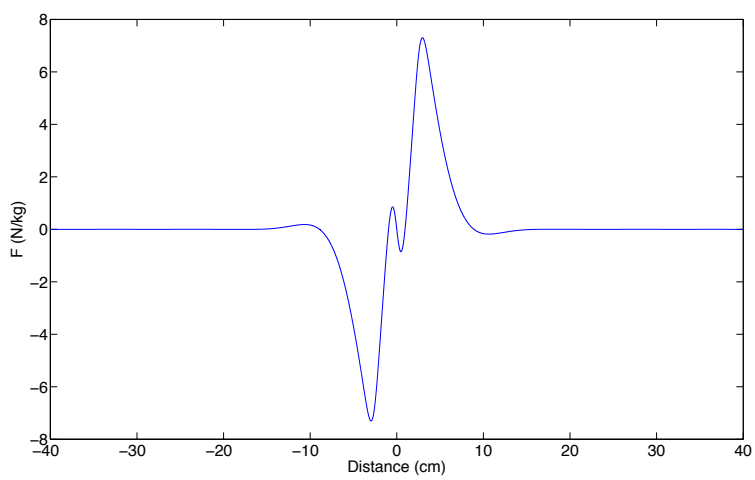

Figure 1.7: Time-averaged electric force as a function of the distance from the center of the flame

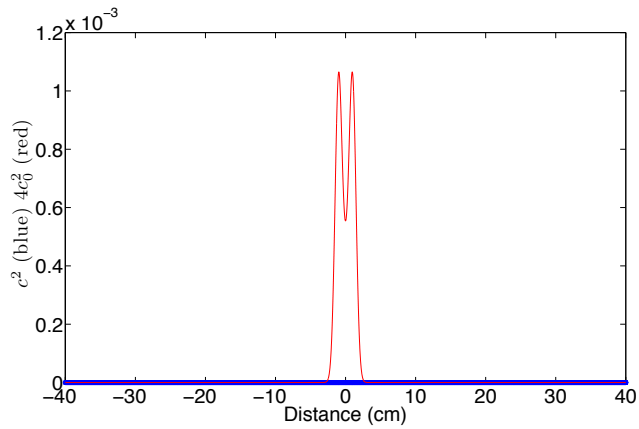

Figure 1.8: Charges separation vs. ions distribution at equilibrium as a function of the distance from the center of the flame. Our assumption that $c^2/4c_o^2 << 1$ is totally justified

noticeable effect to be observed. The experiments made with a point electrode and which lead to the extinction of the flame (Figure 1.1) correspond to the same physical phenomena, but without left-right symmetry, the force is only directed one way and bends the flame so much that it puts it out.

A look at equation 1.8 shows that the dynamics of the charges is determined by a fluctuation term $\vec{\nabla}.(D\vec{\nabla}c)$ and a dissipative term $\vec{\nabla}.(\frac{2qeD}{kT}c_o\vec{E})$. We see that the fluctuation term is the one that creates the necessary dephasing between the the field $E(x,t)$ and the concentration $c(x,t)$ for the force $F(x,t) = E(x,t)c(x,t)$ to have a non-zero time average.

Looking more at the system 1.8 and 1.9 we see that if (E, c) is solution with boundary condition $E(x,t) \to 1$ as $x \to \pm L$, then so is $(\lambda E, \lambda c)$ with boundary condition $E(x,t) \to \lambda$ as $x \to \pm L$ for any real λ. This means that the electric force, product of the field by the concentration, must scale like E_o^2. This scaling can be checked experimentally by measuring the velocity of the gas jets shown in Figure 1.3. Indeed, conservation of momentum for the jets yields: $u\frac{du}{dx} = f$ or $\frac{1}{2}\frac{d}{dx}u^2 = f$, where u is the horizontal velocity of the gas and f the time-averaged force per unit mass. The velocity is given by

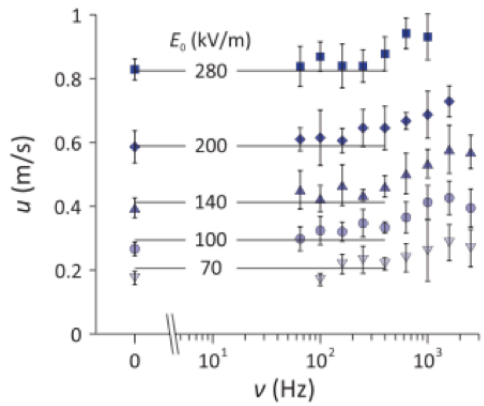

Figure 1.9: Jets velocity measurements, taken from Drews et al [6]

the formula:

$$u = (2 \int f(x)dx)^{1/2} \tag{1.12}$$

This expression can be evaluated numerically but a little bit of analysis can reveal how the velocity scales. Let c_m and ξ be the amplitude and the length respectively of the charges distribution in the presence of the electric field. Then we can write:

$$\frac{E_0}{\xi} \sim \frac{c_m}{\varepsilon_0} \quad \text{and} \quad \int f(x)dx \sim E_0\, c_m\, \xi \tag{1.13}$$

from where it follows that the velocity is given by

$$u \sim E_0 \sqrt{2\varepsilon_0} \tag{1.14}$$

and the constant of proportionality (0.7) can be found by comparing to the numerical computation of the integral. The linear scaling with the imposed field E_0 corresponds to the experiments, see Figure 1.9. The numerical values are also remarkably close, see Figures 1.10 and 1.9.

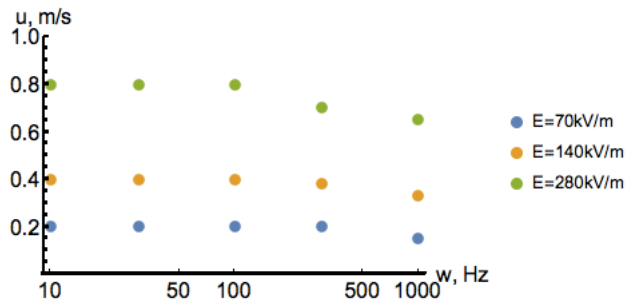

Figure 1.10: Jets velocity computation

In summary, our simple model captures the essence of the interaction between alternating electric fields and flames. It allows to identify the key physical process for a non-zero time-averaged force to be created: the diffusion of the charges. The expression obtained for the electric force agrees quantitatively with the experiments.

2

Viscous boundary layer of splashing drops

Ever since the publication of Worthington's photographs of drops and solid balls falling in deep liquid pools,[34] splash has been the subject of many scientific investigations. Aside from the fundamental interest in understanding such an ubiquitous phenomenon, there are many relevant questions for applications as varied as crop-spraying, inkjet printing, or aerodynamics to give just a few examples.[37] Following Mandre and Brenner,[20,21] by "splash" we mean the rapid event occurring when a droplet

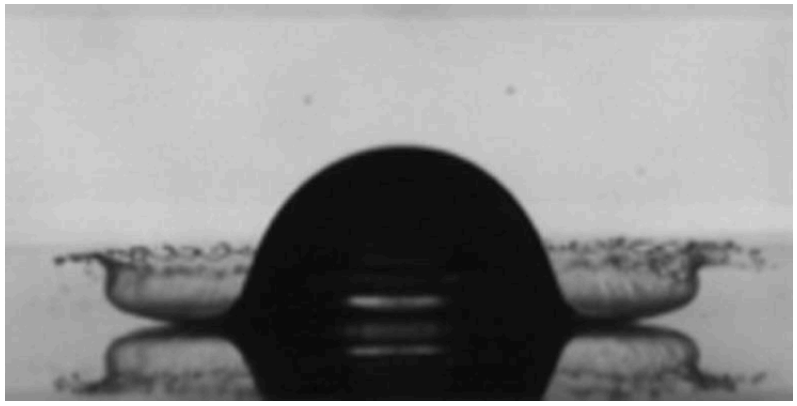

Figure 2.1: Sheet ejection and early disintegration, taken from Xu *et al*[36]

hits a surface and produces a thin fluid sheet that spreads and disintegrates into a spray of droplets. This sheet was identified already half a century ago[2] but there is still no solid theoretical understanding of its origin.

The most prevalent explanation for the ejection of the sheet is based on the singularity that exists when a parabola intersects a plane. In time t, a drop of radius R and velocity V would fall a distance Vt if it could move unhindered by the plane. Using the parabolic approximation for the bottom of the drop, the radius of the wetted region is given by $r = \sqrt{2RVT}$ and its boundary moves at velocity $dr/dt = \sqrt{RV/2t}$. We see that at the very onset of impact, when $t \to 0$, the velocity diverges. The velocity being larger than the liquid sound velocity, the pressure disturbance due to the impact is pinned at the contact line. Very fast, as time increases, dr/dt decreases. Once it is lower than the sound velocity, the abrupt increase in pressure at the liquid-gas interface could be the reason behind the sheet formation.[19,25,13] But this approach suggests that the sheet should be propelled along the solid surface and not launched in the surrounding gas as we see on Figure 2.1. The time scale it predicts for the sheet generation - $t_{sheet} = RV/2c^2$, typically a nanosecond - is much smaller than what is observed. These issues plus the unexpected finding of Xu *et al*[36] that the splash threshold depends on the ambient air pressure, led Mani, Mandre and Brenner[21,20] to develop a theory in which the liquid sheet would

originate because of the interaction between the drop and the intervening gas layer even *before* contact. This theory predicts a negligible role for the viscosity of the liquid, however, experiments seem to indicate that it can have a role.[15] We show here that the viscous boundary layer thickness grows fast enough to cause the assumption of the calculation to break down in many cases. Once this happened, a full calculation needs to be carried out in order to understand the role of viscosity. In a first part we briefly present the main findings of Mandre and Brenner. We then go on to compute the viscous boundary layer's thickness. We then conclude as to when viscosity can be neglected and when more computation is required.

2.1 The self-similar approach to contact

In their papers, Mani, Mandre and Brenner study both compressible and incompressible air regimes. We refer the reader to the papers for all the details.[21,20] Here we will just briefly state those results that are relevant for the computation of the viscous boundary layer's thickness. In particular we only consider the incompressible regime, a reasonable choice for air at 1 bar.

As the drop gets closer and closer to the surface, pressure builds up in the intervening gas layer. At a critical height, that pressure will match the inertial pressure in the drop. A stagnation point at the bottom of the drop appears and the drop starts to deform. It can be shown that the fall of the drop and its subsequent deformations are self-similar with decreasing length scale $l(t)$. Letting h_{min} be the minimum air gap, the maximum air pressure p_{max}, velocity u_{max}, and curvature $h_{xx,max}$ obey the following power laws:

$$p_{max} \sim h_{min}^{-1/2} \qquad u_{max} \sim h_{min}^{-1/2} \qquad h_{xx,max} \sim h_{min}^{-2} \qquad l \sim h_{min}^{3/2} \tag{2.1}$$

Because of the divergence as h_{min} goes to zero, terms that were initially negligible (inertia, surface tension, liquid viscosity, gas compressibility and non-continuum effects) grow rapidly and can poten-

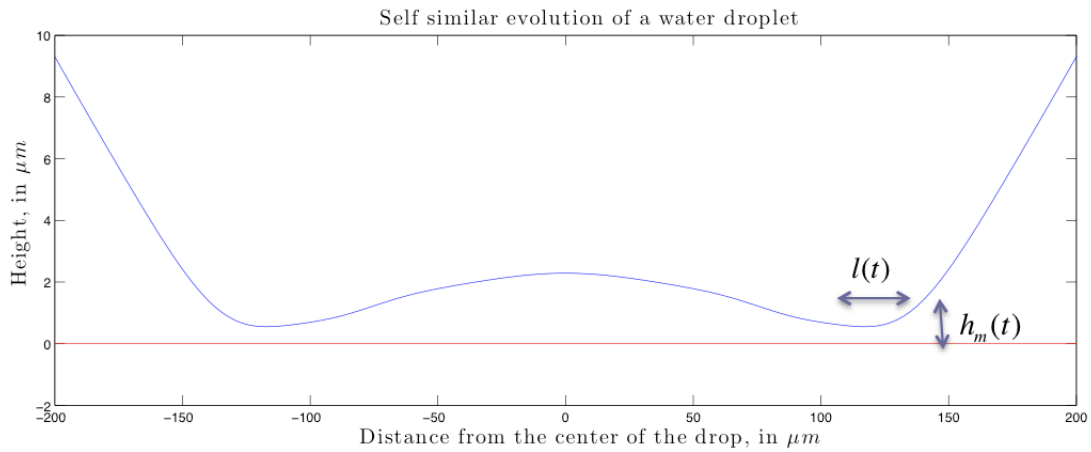

Figure 2.2: Illustration of the self-similar evolution of a 3mm. radius water droplet before contact

tially take over the dynamics. For fast impacts, nonlinear advection dominates and causes the interface to overturn, ejecting a sheet. For slower impacts, surface tension dominates and the drop spreads on a thick film of air. Viscosity was found to remain asymptotically negligible as explained in appendix B of the paper.[20] This result relies on the assumption that the viscous effects are localized in a thin boundary layer. This assumption can only be valid as long as the boundary layer's thickness is smaller than all the other length scales in the problem. The boundary layer thickness grows in time while the self-similar dynamical length scale $l(t)$ decreases. It is not obvious whether there will not be a crossover before surface tension or inertia takes over the dynamics. In such a case viscosity cannot be a priori ignored and a calculation with the full viscous term in the equations must be carried out. In the next section we explain how we compute the evolution in time of the boundary layer's thickness.

2.2 The boundary layer's thickness

One way to compute the boundary layer's thickness is to realize that the boundary layer is the region of space where viscous effects are felt, particularly where the velocity fields with and without viscosity

differ. We therefore propose to compute the difference between the two velocity fields and determine the typical length over which it goes to zero. We use the conventions of the paper by Mandre and Brenner[20] and their non-dimensionalizations.

Let $u_b(x, y, t)$ be the horizontal velocity field of the drop in the boundary layer approximation. Neglecting non-linear inertia, the horizontal component satisfies the following equation:

$$\frac{\partial u_b}{\partial t} = -\frac{\partial \Pi}{\partial x} + \frac{1}{Re}\frac{\partial^2 u_b}{\partial y^2} \tag{2.2}$$

It must also meet a stress condition at the interface with the gas

$$-\mu_l \frac{\partial u_b}{\partial y} = \mu_g \frac{\partial u_g}{\partial y} \text{ at } y = St^{1/3} h(x, t) \tag{2.3}$$

where u_g is the gas velocity. This velocity can be found by integrating the lubrication equation:

$$\frac{\partial^2 u_g}{\partial y^2} = \frac{1}{St}\frac{\partial p}{\partial x} \tag{2.4}$$

with the no-slip boundary condition: $u_g = 0$ at the solid interface and $u_g = u_0$ at the liquid interface, where u_0 is an unknown function.

This leads to

$$\frac{\partial u_g}{\partial y} = \frac{1}{2St^{2/3}}\frac{\partial p}{\partial x} h + \frac{u_0}{St^{1/3} h} \tag{2.5}$$

We study the limit $St \to 0$ and neglect terms of order $O(St^{1/3})$. We thus neglect the last term in the equation above and impose the boundary condition at $y = 0$ instead of $y = St^{1/3} h(x, t)$.

The equations for u_b then simplifies to:

$$\frac{\partial u_b}{\partial t} = -\frac{\partial \Pi}{\partial x} + \frac{1}{Re}\frac{\partial^2 u_b}{\partial y^2} \tag{2.6}$$

and

$$\frac{\partial u_b}{\partial y} = -\frac{\mu_g}{2\mu St^{2/3}}\frac{\partial p}{\partial x}h \text{ at } y = 0 \tag{2.7}$$

On the other hand, let $u(x, y, t)$ be the horizontal velocity field when we don't impose viscous stress at $y = 0$. It satisfies:

$$\frac{\partial u}{\partial t} = -\frac{\partial \Pi'}{\partial x} + \frac{1}{Re}\frac{\partial^2 u}{\partial y^2} \tag{2.8}$$

$$\frac{\partial u}{\partial y} = 0 \text{ at } y = 0 \tag{2.9}$$

The effects of the viscous stress are only felt in the boundary layer and so, outside of it: $\Pi' = \Pi$. Since transverse pressure variations are neglected in the boundary layer ($\partial\Pi/\partial y = 0$) we can say that $\Pi' = \Pi$ everywhere.

This allows us to look at the following diffusion equation for the difference in the fluid velocities: $\Psi = u_b - u$:

$$\frac{\partial \Psi}{\partial t} = \frac{1}{Re}\frac{\partial^2 \Psi}{\partial y^2} \tag{2.10}$$

with the boundary conditions

$$\frac{\partial \Psi}{\partial y} = -\frac{\mu_g}{2\mu St^{2/3}}\frac{\partial p}{\partial x}h \text{ at } y = 0 \text{ and } \Psi = 0 \text{ when } y \to \infty \tag{2.11}$$

Realizing that $\mu_g/\mu = ReSt$ we can simplify the first boundary condition and obtain:

$$\frac{\partial \Psi}{\partial y} = -\frac{1}{2}ReSt^{1/3}\frac{\partial p}{\partial x}h \text{ at } y = 0 \text{ and } \Psi = 0 \text{ when } y \to \infty \tag{2.12}$$

In order to solve equations 2.10 and 2.11 we need to have $\Psi(x, y, t = 0)$. This is of course 0.

Using the method of images for the upper half plane we find that Ψ is given by:

$$\Psi(x, y, t) = \frac{St^{1/3}}{2} \int_0^t G(y, t, t')h(x, t')\frac{\partial p}{\partial x}(x, t')dt' \tag{2.13}$$

where the Green function is :

$$G(y, t, t') = \sqrt{\frac{Re}{\pi(t - t')}} \exp -(\frac{Re\, y^2}{4(t - t')}) \tag{2.14}$$

Changing variables $t \to s = 2\sqrt{t - t'}$ and letting $f = h\frac{\partial p}{\partial x}$.

$$\Psi(x, y, t) = \frac{St^{1/3}\sqrt{Re}}{2\sqrt{\pi}} \int_0^{2\sqrt{t}} \exp -(\frac{Re\, y^2}{s^2})f(x, s)ds \tag{2.15}$$

The typical length over which Ψ goes to 0 in the y direction, can be evaluated the following way:

$$\delta(x, t) = \frac{\int_0^\infty y\Psi(x, y, t)dy}{\int_0^\infty \Psi(x, y, t)dy} \tag{2.16}$$

With a little bit of algebra we obtain:

$$\delta(x, t) = \frac{1}{\sqrt{\pi Re}} \frac{\int_0^{2\sqrt{t}} s^2 f(x, s)ds}{\int_0^{2\sqrt{t}} sf(x, s)ds} \tag{2.17}$$

We previously defined $f(x, t') = h(x, t')\frac{\partial p}{\partial x}(x, t')$. We expect $f(x, t')$ to give a contribution only for times $t' > t_r$, where t_r is the time the dimple forms. That's when the self similar evolution starts and the following laws hold:

$$h_{min} \sim (t^* - t')^{2/3} \qquad p_{max} \sim (t^* - t')^{-1/3} \qquad l \sim (t^* - t') \tag{2.18}$$

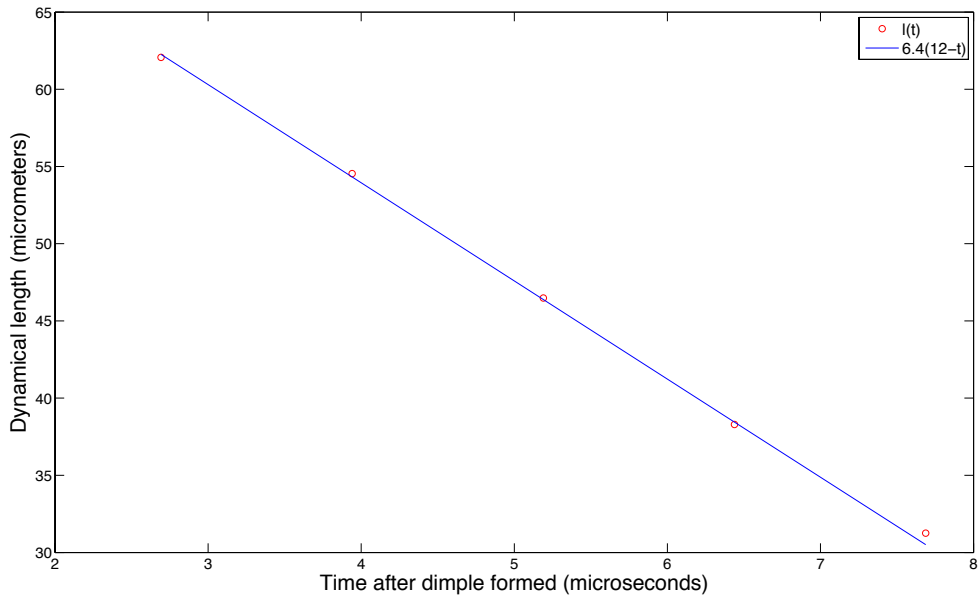

Figure 2.3: Decrease of the dynamical length $l(t)$ and fit that allows to find the blow-up time t^* and the coefficient for the laws 2.18

where t^* is the blow-up time of the self-similar solution. t^* and the coefficients that appear in 2.18 can be found from the numerical simulation. See Figure 2.3 for an illustration.

We therefore have

$$f(x, t') \sim (t^* - t')^{-2/3} \tag{2.19}$$

We evaluate the length $\delta(x, t)$ at x such that $h = h_{min}$ and so we use expression 2.19 and the fact that $s = 2\sqrt{t - t'}$ to compute the integrals in equation 2.17. We obtain:

$$\delta(t) = \frac{4}{\sqrt{\pi Re}} J_1/J_2 \sqrt{t^* - t} \tag{2.20}$$

where

$$J_1 = \int_0^{\sqrt{(t-t_r)/(t^*-t)}} \frac{x^2 dx}{(1+x^2)^{2/3}} \quad \text{and} \quad J_2 = \int_0^{(t-t_r)/(t^*-t)} \frac{dx}{(1+x)^{2/3}} \tag{2.21}$$

Computing J_2 is straightforward with the change of variable $u = (1+x)^{2/3}$

$$J_2 = \int_1^{((t^*-t_r)/(t^*-t))^{2/3}} \frac{3du}{2\sqrt{u}} = 3((\frac{t^*-t_r}{t^*-t})^{1/3} - 1) \tag{2.22}$$

J_1 must be computed numerically. It should be noted that in order to make the computation easier with Mathematica, it is best to use the following expression obtained after an integration by part:

$$J_1 = \frac{3}{2}\sqrt{\frac{t-t_r}{t^*-t}}(\frac{t^*-t_r}{t^*-t})^{1/3} - \frac{3}{2}\int_0^{\sqrt{(t-t_r)/(t^*-t)}} (1+x^2)^{1/3} dx \tag{2.23}$$

2.3 Boundary layer's thickness and dynamical length crossover

Determining the blow-up time by fitting the self-similar regime like in Figure 2.3 we have all that is necessary to compute the boundary layer's thickness for a given drop. Figure 2.4 shows the growth of the boundary layer for a very viscous silicone oil. About $4\mu s$ after the dimple formed,the viscous region becomes bigger than l. Using the expressions for the height at which surface tension or nonlinear advection set in ($5\,\delta^{2/3}$ and $60\,St^{2/3}$ respectively[20]) one can check that this is still in the self similar regime.

Figure 2.4 shows the crossover for a very viscous fluid, but even for water, the crossover happens during the self-similar regime for a very wide range of drops' sizes and impact velocities. See Figure 2.5.

This phase diagram clearly shows that the boundary layer's growth must be taken into account to analyze splash. This does not mean that viscosity necessarily plays a role, rather it means that the question of its role and its extent can only be answered by a computation that takes the full viscous

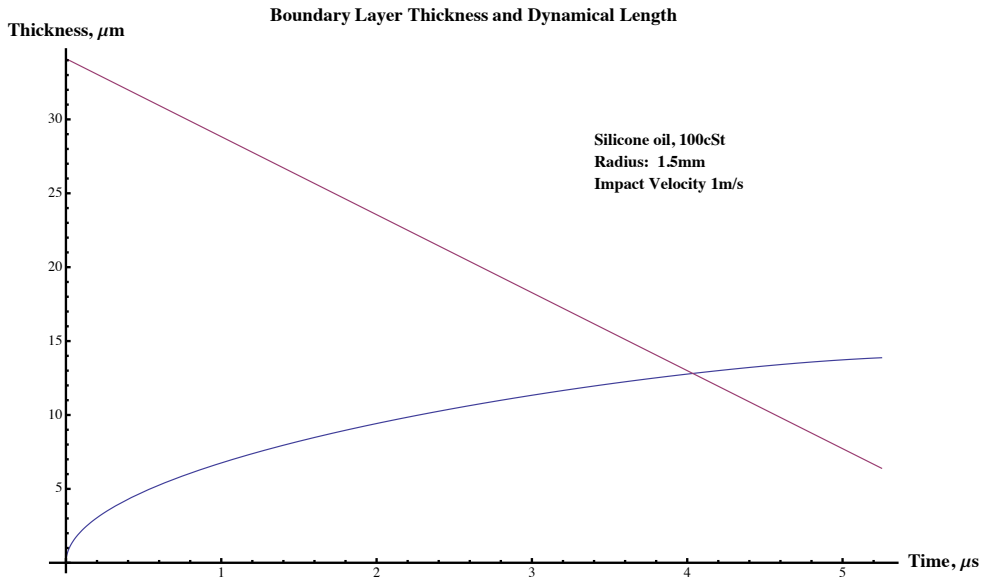

Figure 2.4: Time evolution of the boundary layer's thickness and of the self-similar dynamical length during a silicone oil drop's splash

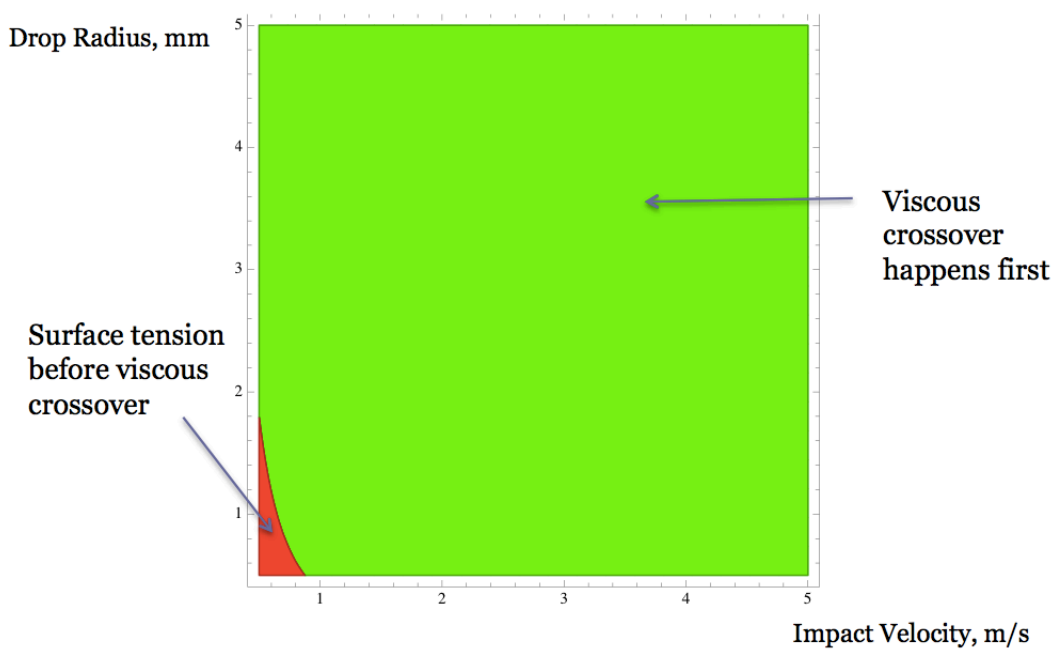

Figure 2.5: Phase diagram for the viscous crossover of a water droplet

term in the equations and not just a boundary layer approximation.

3

Microdroplets generation in the centipede device

Microdroplets are used more and more in a wide variety of applications: to conduct chemical reactions in picoliter volumes [4], as biological screening assays [28,12] or as templates to produce calibrated microparticles [7] and microcapsules of active ingredients [5]. The accuracy of the screening assays as well as

the degree of control over the chemical reactions and the release kinetics of active ingredients critically depend on a very narrow size distribution for the microdroplets. In addition, a very large number of drops is required. Unfortunately, high throughput methods, such as high-pressure homogenization, offer limited control over the drop size.[9,14] Microfluidics methods with better control of drop size have emerged,[29,30] like step membrane emulsification.[31,27] These methods however have a lower throughput, limiting their applicability to high-end products sold in moderate quantities. The throughput can be increased if many drop makers are run in parallel.[22,26] However, parallelization compromises the robustness of the operation as the failure of a single drop maker typically results in the failure of the entire device. Moreover, inevitable fluctuations of the flux from channel to channel lead to variations in the drops' sizes.

In 2013, Doctor Esther Amstad, from Professor David Weitz' laboratory at Harvard University introduced a device that is both robust in its operation and produces monodisperse drops at a high throughput in a single emulsification step. This device, called centipede because of its hundreds of parallel channels, allows the use of microdroplets for a much broader range of applications. A single device takes up a volume of 100 mm^3 and can produce up to $150 mL/h$ of monodisperse microdroplets: size variations remain below 3 %. In what follows we explain the mechanism through which it produces drops, this allows us to understand how the drops' size is related to the device's parameters and what the maximum flux is.

3.1 The centipede device

The device is made of polydimethylsiloxane (PDMS) using soft lithography[35]. The inner phase is injected into a long central channel, while the outer phase is injected in the side channels. The channels are connected through hundreds of small drop makers as shown on Figure 3.2. The drop makers are made in such a way that at the orifice the height goes up by an order of magnitude. Drops exit through

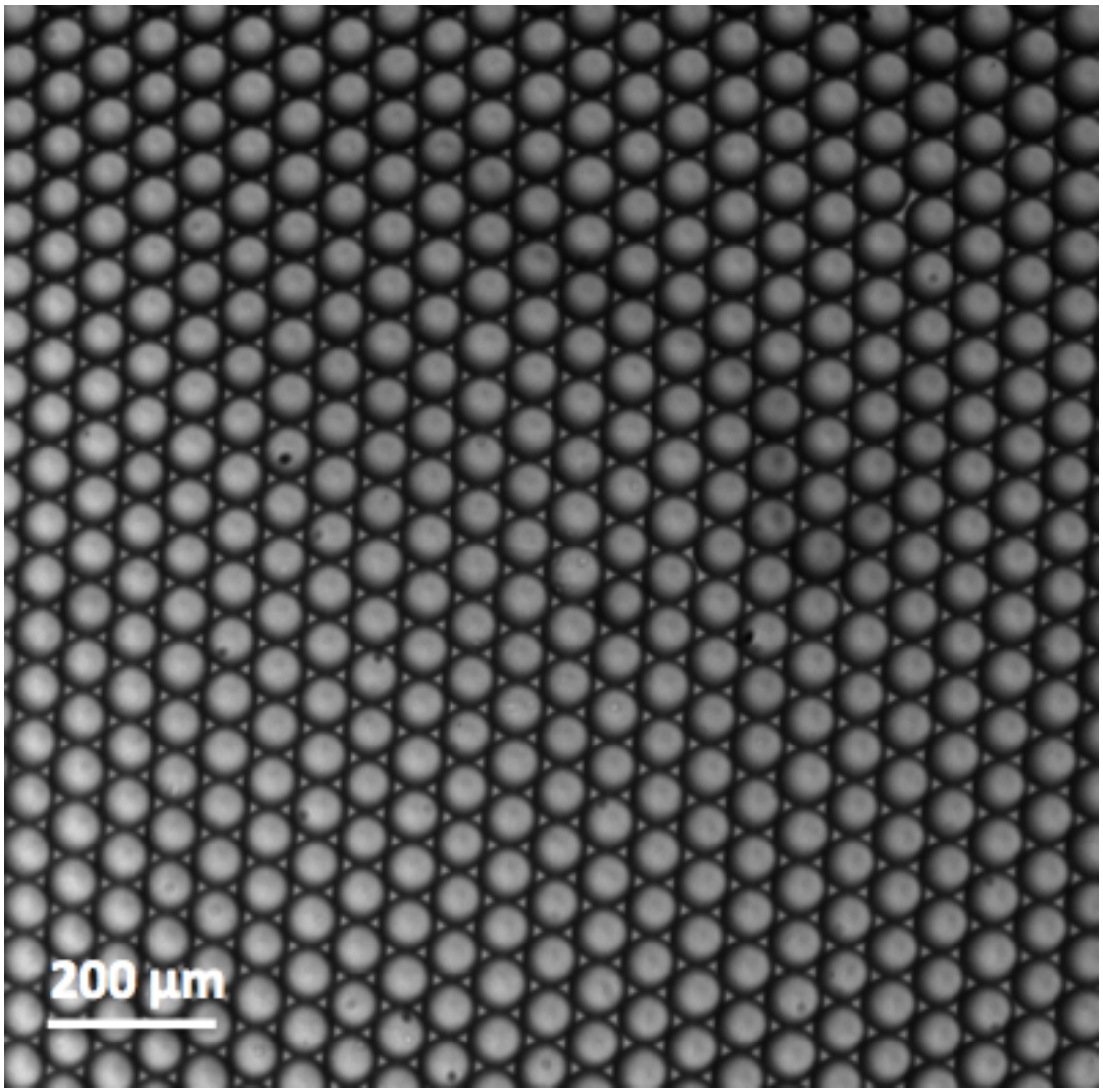

Figure 3.1: Optical micrograph of drops produced by a centipede device

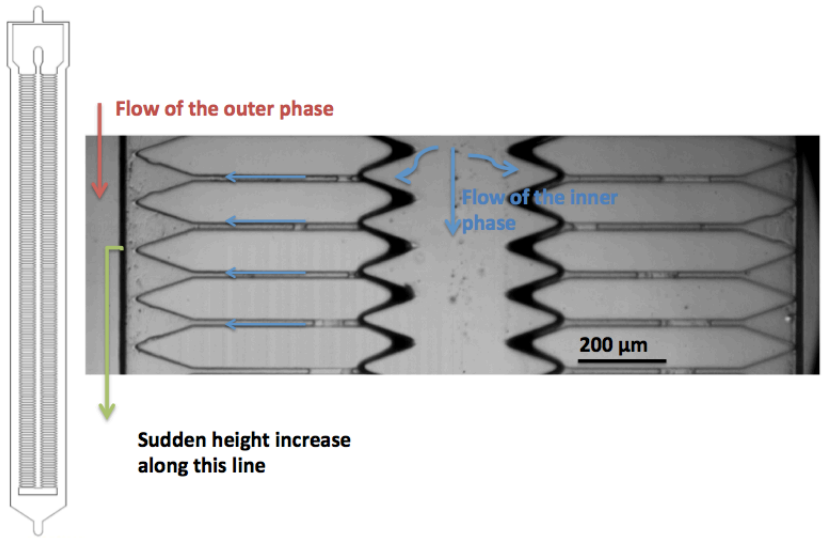

Figure 3.2: Optical micrograph of the drop makers

a single outlet located downstream. Figure 3.3 shows the parameters of the device.

The size of the drops is not affected by changing the flux of either the inner or the outer phase, as shown on Figure 3.5. This led us to suspect that the drops are not produced in a dynamic process but as a result of an instability or a curvature matching incompatibility in a quasi-static flow. We simulated the fluid in one droplet maker of the centipede using Surface Evolver, a program that computes the equilibrium configurations of fluids under different geometric and physical constraints*. The code is given in Appendix B. During the initial stages of the drop formation, the simulated shape of the evolving drop closely resembles the experimental observations. Past a certain critical volume, which depends on the drop maker's parameters, Surface Evolver is unable to find an equilibrium configuration. This confirms our assumption of a sudden breakup in a quasi-static flow. To better understand what happens we study the first phase of the flow, before we reach the critical volume.

*For more information see http://www.susqu.edu/brakke/evolver/evolver.html

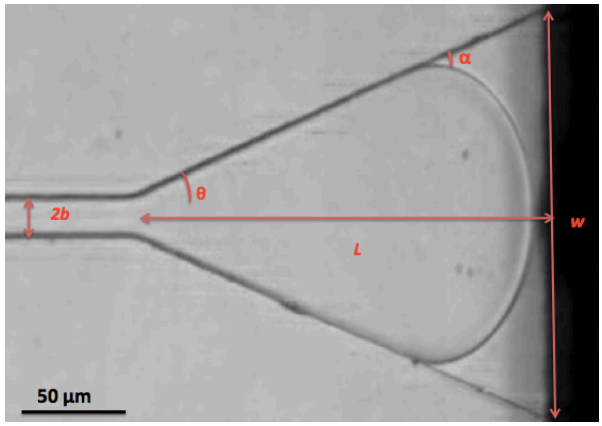

Figure 3.3: Parameters of a centipede device's drop maker

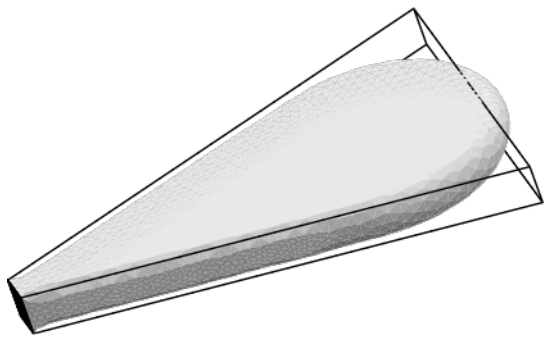

Figure 3.4: Simulation of the fluid in the drop maker, just below the volume at which there is no more stable solution

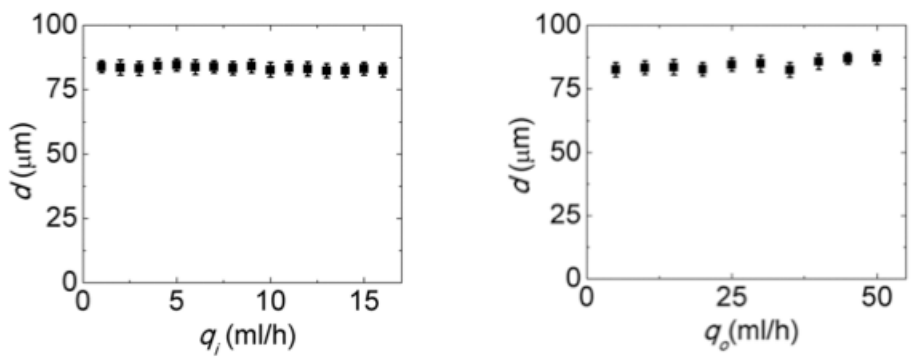

Figure 3.5: Influence of the inner (q_i) and outer (q_o) flux on the drop's size

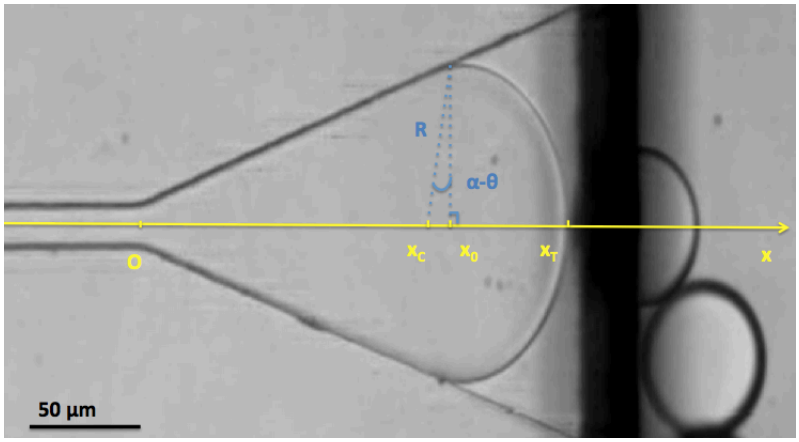

Figure 3.6: Determination of the tongue radius

3.2 The breakup mechanism

The fluid adopts a tongue shape inside the channel; its radius in the horizontal plane $R(x_T)$ can be expressed as a function of the device's parameters and the fluid's contact angle with the walls α. x_T is the coordinate of the tip of the tongue as measured on a horizontal axis going through the middle of the drop maker and starting where the walls begin to open.

Looking at Figure 3.6 we see that:

$$\cos(\alpha - \vartheta) = \frac{(b + x_0 \tan\vartheta)}{R(x_T)} \quad \text{and} \quad R(x_T)\sin(\alpha - \vartheta) + (x_T - x_0) = R(x_T) \tag{3.1}$$

We can solve for the radius:

$$R(x_T) = \frac{b + x_T \tan\vartheta}{\cos(\alpha - \vartheta) + \tan\vartheta\,(1 - \sin(\alpha - \vartheta))} \tag{3.2}$$

Once the fluid passes the edge of the orifice and enters the tall channel of the continuous phase, a drop precursor forms. The section in the plane of the orifice links the two parts of the body: the tongue inside the device and the droplet precursor outside. A look at this section in Surface Evolver

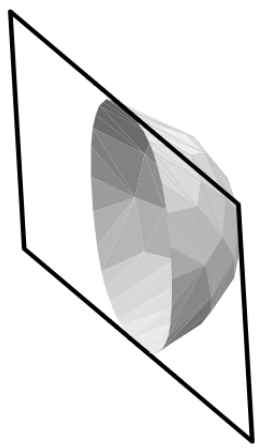

Figure 3.7: Drop precursor bulging out (simulation)

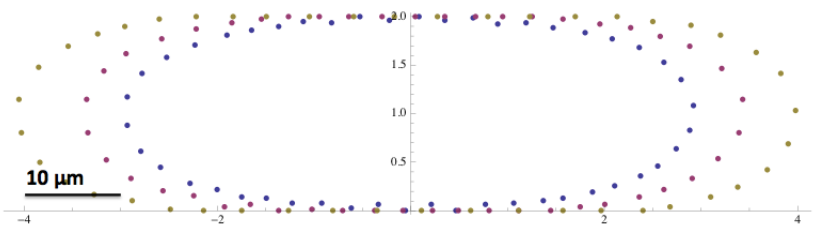

Figure 3.8: Growth of the elliptic section until breakup

suggests that it has an elliptic shape. This obviously comes from the aspect ratio of the device; a square capillary would have given a circular section. As more fluid is injected, the ellipse's axes grow until it reaches the top and bottom walls. It then becomes flattened as it continues to expand in the lateral direction.

Once the drop precursor appears, it is more convenient to parametrize the problem with a, the semi-major axis of the ellipse than x_T. They are related by $x_T = L + R(x_T) - \sqrt{R(x_T)^2 - a^2}$. Injecting this expression in 3.2 and solving for R, we get:

$$R(a) = \frac{A(1-v) - v\sqrt{A^2 + a^2(2v-1)}}{1-2v} \tag{3.3}$$

with

$$\mathcal{A} = \frac{b + \tan\vartheta\, L}{\cos(\alpha - \vartheta) + \tan\vartheta(1 - \sin(\alpha - \vartheta))} \quad \text{and} \quad v = \frac{\tan\vartheta}{\cos(\alpha - \vartheta) + \tan\vartheta(1 - \sin(\alpha - \vartheta))}$$

One can check that this expression for $R(a)$ is always well-defined and greater than a for all values of a such that $2a$ is smaller than the total width of the device and for all values of ϑ in the typical range used for the drop makers (5°-45°). This rules out a matching incompatibility as the cause for breakup. In fact as we proceed to explain, the drop detaches because of an instability. The points on opposite sides of the flattened ellipse are linked by arcs of circles. Their radius, r, is found by imposing the constant mean curvature condition. The mean curvature of the fluid outside the drop maker is $1/2r$ while inside we have two contributing terms: the curvature in the horizontal plane $1/R(a)$ and the curvature in the vertical plane $2\cos\alpha/h$, where h is the height of the drop maker.

$$\frac{1}{r} = \frac{2\cos\alpha}{h} + \frac{1}{R(a)} \tag{3.4}$$

The surface of the fluid outside locally looks like a half-cylinder of length $2a$ and radius r. As a increases over time, the cylinder becomes prone to a Rayleigh-Taylor instability. As detailed by Rayleigh in his paper,[24] the ratio of wavelength to diameter for the kind of disturbance which leads most rapidly to the disintegration of the cylindrical mass is $\lambda/2r \approx 4.5$ which for our case would predict a breakup when $a/r \approx 4.5$. This is indeed the ratio at which the simulation in Surface Evolver cannot any more find a stable configuration for the fluid. Figure 3.9 shows the ratio found numerically for different device parameters. The variations around the theoretical prediction of 4.5 are probably due to finite-size effects. This result clearly identifies a Rayleigh-Taylor instability as the mechanism for droplet breakup in the centipede device.

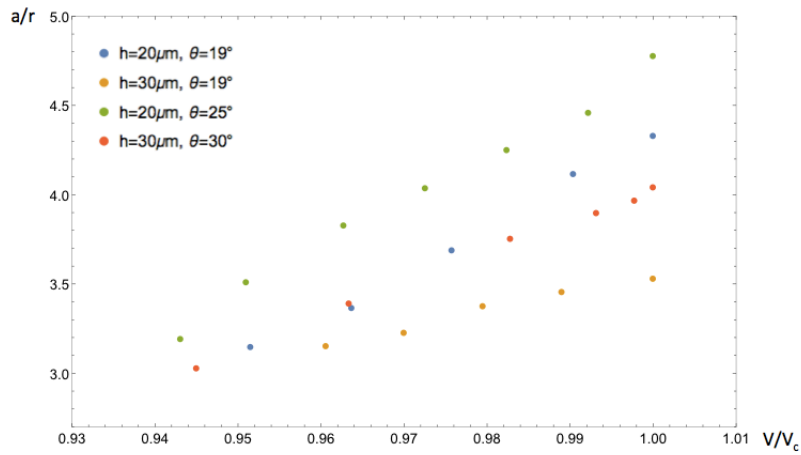

Figure 3.9: Ratio a/r as V increases to the breakup volume V_c.

3.3 The drop's size

Identifying the breakup mechanism allows us to understand how the drop's radius scales with the device's parameters. Indeed we know that the fluid that detaches has approximately the shape of a half-cylinder with radius r given by equation 3.4 and total length $9r$. This volume corresponds to a spherical droplet of radius $r_d = 3\,r/2$. Because we are interested in producing small droplets, the devices we work with are very thin and so in equation 3.4 it is the first term that dominates, i.e. $r \approx h/2\cos\alpha$. This gives us the following formula for the drop's radius:

$$r_d = \frac{3h}{4\cos\alpha} \tag{3.5}$$

The linear scaling with the device's height is in agreement with experimental results as shown on Figure 3.10

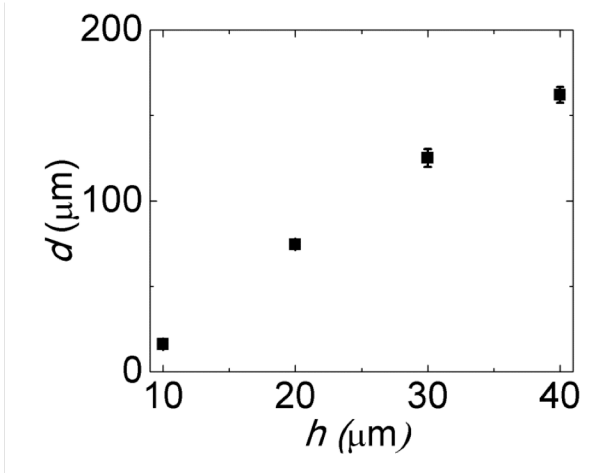

Figure 3.10: Drop's diameter as a function of the centipede's height

3.4 Size limit

Many applications require very small drops and thus it is important to know if there is a lower limit on the size of the drops we can produce with the centipede. Equation 3.5 suggests that all that is required is to decrease the centipede's height. However experiments reveal that below a certain value, the device fails to produce monodisperse drops, suggesting that our theoretical analysis is no more valid. For the instability to occur in a quasi-static regime, the time it takes for the drop to breakup must be smaller than the time it takes to reach the critical volume at which the drop becomes unstable. From Rayleigh's analysis, the time associated with the most unstable mode is given by $\tau_R \approx 3\sqrt{\varrho h^3/\sigma}$. The time it takes to reach the critical volume from the moment the fluid comes out of the drop maker is given by $\tau_V \approx V_d/q$ where V_d is the volume of the produced drop and q is the flux at which the inner phase is injected. Using the formula 3.5 to compute V_d, we get the following condition relating the flux to the height:

$$q < \frac{1}{1.7\cos^3\alpha}\sqrt{\frac{\sigma}{\varrho}}h^{3/2} \tag{3.6}$$

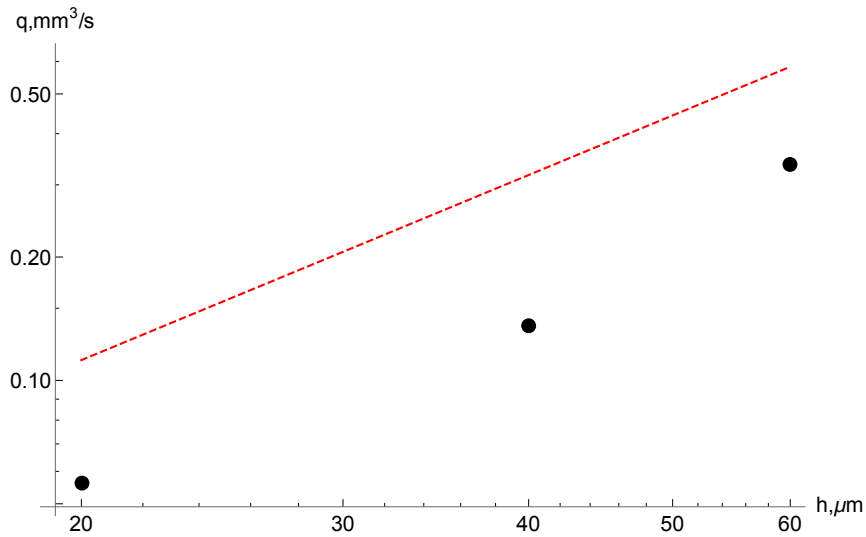

Figure 3.11: Maximum flux as a function of the centipede's height

The 3/2 power law matches very well the observations for the maximum flux as a function of the height as reported on Figure 3.11.

The centipede is the first device capable of producing monodisperse microdroplets at a high rate. This comes from the mechanism responsible for the drop's detachment: an instability in an otherwise quasi-static flow. Packing the devices into 1 dm^3 one can produce 40 liters of 15 μm drops per hour or 800 liters of 160 μm drops, and as much as 4700 liters of 260 μm drops. Using the centipede allows one to widen the range of applications of microdroplets to products sold in the several thousands of tons annually.

A

Combustion Code

Here is the code used to solve the equations of Chapter 1. There are three files: a main.m file which calls the solver, flameode.m which contains the equations and flamebc.m which contains the boundary conditions

```
%%%%%%%%%%%%%%%%%%%%%%% FILE MAIN.M %%%%%%%%%%%%%%%%%%%%%%%%%%%%%%%
% This program solves the system of ODEs to compute the charge
% concentration and electric field for a flame in a capacitor. The
% derivation of the equations is explained in the thesis.
% Lengths are measured in units of the flame front width l0=1e-4m.
clear
close all
clc
%  'infinity' is the end of the x axis. We don't need to go as far as L.
infinity =3000;
%  The constant guess for the solution satisfies the boundary conditions.
solinit = bvpinit(linspace(-infinity,infinity,2000),[0 1 1]);
sol = bvp4c(@flameode,@flamebc,solinit);
%Now we take the solution we just found and use it as a guess.
options=bvpset('RelTol', 1e-4);
sol = bvp4c(@flameode,@flamebc,sol,options);
a = linspace(-infinity,-200,10000);
b=linspace(-200,200,40000);
c = linspace(200,infinity,10000);
x=[a,b,c];
f = deval(sol,x);
% f is the solution of the equation: f(1,:) is the charge concentration c
% and f(3,:) is the electric field
q=1; % valence of the ions
E0=3e5; % amplitude of the field (V/m)
e=1.6e-19; % elcetric charge (C)
cm=q*e*1e17; % typical charge density due to one species (C/m3)
```

```
p0=1e5; %atmospheric pressure (IS)
M=29e-3; %molar mass of air (kg)
R=8; % ideal gas consant (IS)
% the temperature
T0=3e2; % the room temerature (in K)
Tm=3e3; % the temperature in the reaction zone (in K)
l0=1e-4; % flame front width in m
l1=1e-2/l0; % location of the flame surface (1cm)
Lt=1e-1/l0; % typical length of the temperature variation (10cm)
% the temperature field
T=1/2*(Tm-T0)*exp(-((x-l1)/Lt).^2)+1/2*(Tm-T0)*exp(-((x+l1)/Lt).^2)+T0;
Tcen=Tm/3*exp(-((x)/l1).^2);
T=T-Tcen;
%the density
rho=p0*M./(R.*T);
% the electric force per unit mass
F=E0*cm./rho./2.*(real(f(1,:)).*real(f(3,:))+imag(f(1,:)).*imag(f(3,:)));


%%%%%%%%%%%%%%%%%%%%%%%% FILE FLAMEODE.M %%%%%%%%%%%%%%
function fprime=flameode(x,f)
%Definition of the parameters used in the equations:
w=1e3; % the frequency of the imposed field (in Hz)
e=1.6e-19;% the electric charge (in C)
T0=3e2;% the room temerature (in K)
Tm=3e3; % the temperature in the reaction zone (in K)
k=1.4e-23; % Boltzmann's constant (IS)
D0=1e-5; % the diffusion constant (m2/s)
```

```
eps0=9e-12; % vacuum permittivity (IS)
l0=1e-4; % flame front width in m
l1=1e-2/l0; % location of the flame surface (1cm)
Lt=1e-1/l0; % typical length of the temperature variation (10cm)
Lc=1e-2/l0; % typical length over which charges are located in the absence of field (1
q=1; % valence of the ions
cm=q*e*1e17; % typical charge density due to one species (C/m3)
E0=3e5; % amplitude of the field (V/m)
% temperature field and its derivative
T=1/2*(Tm-T0)*exp(-((x-l1)/Lt).^2)+1/2*(Tm-T0)*exp(-((x+l1)/Lt).^2)+T0;
Tcen=Tm/3*exp(-((x)/l1).^2);
T=T-Tcen;
dTcen=-2*Tm/3*x./l1.*exp(-((x)/l1).^2);
dT=-(Tm-T0)*(x-l1)/Lt.*exp(-((x-l1)/Lt).^2)-(x+l1)/Lt.*(Tm-T0).*exp(-((x+l1)/Lt).^2);
dT=dT-dTcen;
% the ions concentration and its derivative, in the absence of field
c0=cm*(exp(-(((x-l1)/Lc).^2))+exp(-(((x+l1)/Lc).^2)));
dc0=cm*(-2*(x-l1)/Lc.*exp(-(((x-l1)/Lc).^2))-2*(x+l1)/Lc.*exp(-(((x+l1)/Lc).^2)));

% the equations
fprime(1)=l0*f(2);
fprime(2)=l0^2*(-1i*w*T0./(T.*D0)+2*q*e*c0./(k*T.*eps0)).*f(1)...
    -1./T.*dT*l0^2*f(2)+2*q*e*E0*l0^2./(k*T*cm).*dc0.*f(3);
fprime(3)=l0/(E0*eps0)*cm*f(1);
fprime=[fprime(1); fprime(2); fprime(3)];

%%%%%%%%%%%%%%%%%%%%%%%%%%%% FILE FLAMEBC.M %%%%%%%%%%%%%%%%
function res = flamebc(f0,finf)
```

```
  res = [f0(1); finf(1); f0(3)-1];
% The concentration is zero at both limits.
% The field is 1 far away on the left, and by symmetry it will also be on the right.
```

B

Surface Evolver code

From Michael Chemama with help from Professor Ken Brakke.

Code simulating the fluid inside a drop maker of the centipede's device.

```
parameter alpha=160 // contact angle of the fluid with the wall.(non wetting case)
//parameter alpha=20 // contact angle of the fluid with the wall. (wetting case)
```

```
parameter theta=19*pi/180 // angle of the device
parameter LL=23.1 // length of the device // units are 10s of microns
parameter aa=2 // initial width and height of the device

parameter xr=LL // x_right, position of the fluid
parameter xl=LL/5 // x_left, position of the fluid

parameter yl=(LL-xl)*tan(theta)+aa/2
parameter yr=(LL-xr)*tan(theta)+aa/2


gravity_constant 0

#define WALLT (-cos(alpha*pi/180)) // virtual tension of facet on plane

constraint 1
formula:z=0

constraint 2
formula: y-(LL-x)*tan(theta)=aa/2

constraint 3
formula:y+(LL-x)*tan(theta)=-aa/2

constraint 4
formula:z=aa

constraint 5
```

```
formula: x=xr

constraint 6 nonnegative
formula:  z=0

constraint 7 nonpositive
formula: y-(LL-x)*tan(theta)=aa/2

constraint 8 nonnegative
formula: y+(LL-x)*tan(theta)=-aa/2

constraint 9 nonpositive
formula: z=aa

// x constraint at the end, to provide a guaranteed ring
// of edges at x = 0, after the liquid protrudes.
constraint end_con
formula: x = 0

// Barrier for filaments at the open end
constraint end_barrier nonnegative
formula: x = 0

// Barrier to prevent liquid coming out the end from backing up
constraint reverse_barrier nonpositive
formula: x = 0

vertices
```

```
// the device
1      0      -LL*tan(theta)-aa/2        0    fixed
2      LL    -aa/2                 0    fixed
3      LL    aa/2                       0    fixed
4      0      LL*tan(theta)+aa/2       0    fixed
5      0      -LL*tan(theta)-aa/2        aa   fixed
6      LL    -aa/2                 aa   fixed
7      LL    aa/2                       aa   fixed
8      0      LL*tan(theta)+aa/2       aa   fixed

// the fluid
9     xl     -yl 0    constraints 1,3,end_barrier
10    xr     -yr 0    constraints 1,3,5    fixed
11    xr     yr  0    constraints 1,2,5    fixed
12    xl     yl  0    constraints 1,2,end_barrier
13    xl     -yl aa   constraints 4,3,end_barrier
14    xr     -yr aa   constraints 4,3,5    fixed
15    xr     yr  aa   constraints 4,2,5    fixed
16    xl     yl  aa   constraints 4,2,end_barrier


edges

// the device
1   1   2   no_refine        fixed    bare
2   2   3   no_refine        fixed    bare
3   3   4   no_refine        fixed    bare
4   4   1   no_refine        fixed    bare
```

```
5   5   6   no_refine       fixed   bare
6   6   7   no_refine       fixed   bare
7   7   8   no_refine       fixed   bare
8   8   5   no_refine       fixed   bare
9   3   7   no_refine       fixed   bare
10  6   2   no_refine       fixed   bare
11  1   5   no_refine       fixed   bare
12  8   4   no_refine       fixed   bare

// the fluid
13      9    10  constraints 1,3
14      10   11  constraint 1        no_refine   fixed
15      11   12  constraints 1,2
16      12   9   constraint 1,   end_barrier
17      13   14  constraints 4,3
18      14   15  constraint 4        no_refine   fixed
19      15   16  constraints 4,2
20      16   13  constraint 4,   end_barrier
21      9    13  constraints 3,      end_barrier
22      16   12  constraints 2,  end_barrier
23      11   15  constraint 2        no_refine   fixed
24      14   10  constraint 3        no_refine   fixed

faces
1   13  14  15  16  tension WALLT   constraint 1
2   17  18  19  20  tension WALLT   constraint 4
3   16  21  -20 22  constraints 6,7,8,9
4   14  23  -18 24  no_refine       fixed
```

```
5   -13 21  17  24  tension WALLT   constraint 3
6   -15 23  19  22  tension WALLT   constraint 2

bodies
1   -1 2 3 4 -5 -6 volume aa*(yr+yl)*(xr-xl)



read

// For non-wetting, remove end_barrier, since it just confuses ringline.
if alpha > 90 then {
   unset vertex constraint end_barrier;
   unset edge constraint end_barrier;
};

// Command to install the x = 0 curve.  Call after liquid
// protrudes from tube.
ringflag := 0 // to make sure ringline is only called once.
ringline := {
  foreach edge ee where not fixed and ee.vertex[1].x*ee.vertex[2].x < 0 do
  { refine ee;
    set ee.vertex[2] constraint end_con;
  };
  set edge ee constraint end_con where sum(ee.vertex,on_constraint end_con) = 2;
  u; u;

  // free exterior part of blob
  foreach vertex vv where x < -1e-5 do
```

```
  { unset vv constraint 6;
    unset vv constraint 7;
    unset vv constraint 8;
    unset vv constraint 9;
    unset vv.edge constraint 6;
    unset vv.edge constraint 7;
    unset vv.edge constraint 8;
    unset vv.edge constraint 9;
    unset vv.facet constraint 6;
    unset vv.facet constraint 7;
    unset vv.facet constraint 8;
    unset vv.facet constraint 9;
  };

  ringflag := 1;

} // end ringline

// Command to keep the mesh nice.
groom := {
  if not ringflag and min(vertex,x) < -0.30*aa  then
  {
    ringline;
  };
  // check for pulling off floor and ceiling
  foreach vertex vv where on_constraint 1 and sum(vv.edge, on_constraint 1) <= 2 do
  { unset vv constraint 1;
    unset vv.edge constraint 1;
```

```
  };
  foreach vertex vv where on_constraint 4 and sum(vv.edge, on_constraint 4) <= 2 do
  { unset vv constraint 4;
    unset vv.edge constraint 4;
  };

  refine edge where length > 0.8;
  u;V;
  delete edge where length < 0.1 and not on_constraint end_con;
  delete facet where area < 0.01 and not on_constraint end_con;
  u; V;

}

// evolve at original volume until corners tunnel back.
gogo := {
  refine edge where not fixed and length > 2; u;
  refine edge where not fixed and length > 1.4; u;
  refine edge where not fixed and length > 1; u;
  refine edge where not fixed and length > 0.6; u;
  {g 10; groom } 80;
}



// Increase volume gradually.  Do this after gogo.
go_more := {
  for ( ; body[1].target < 3*volu ; body[1].target *= 1.01 )
```

```
  {
     { g 10; groom } 5;

     if min(vertex,z) < -1.2*aa then // breakout of blob
       break;
  };

  // Evolve at constant volume. May break into pieces, which
  // is why "rebody" is in here.
  { g 10; groom; rebody } 70;
}
```

References

[1] Bone, W. A., Fraser, R. P., & Wheeler, W. H. (1931). *Proc. Roy. Soc. A*, 132, 1.

[2] Bowden, F. P. & Field, J. E. (1964). The deformation of solids by liquid impact, by solid impact and by shock. *Proc. R. Soc. Lond. A*, 282, 331.

[3] Calcote, H. F., Kurzius, S. C., & Miller, W. J. (1965). Negative and secondary ion formation in low-pressure flames. In *Tenth Symposium on combustion* (pp. 605). Pittsburgh: The Combustion Institute.

[4] Cho, S., Kang, D. K., Choo, J., deMello, A. J., & Chang, S. I. (2011). Recent advances in microfluidic technologies for biochemistry and molecular biology. *BMB reports*, 44, 705.

[5] Datta, S. S., Abbaspourrad, A., Amstad, E., Fan, J., Kim, S. H., Romanowsky, M., Shum, H. C., Sun, B., Utada, A. S., Windbergs, M., Zhou, S., & Weitz, D. A. (2014). 25th anniversary article: Double emulsion templated solid microcapsules: Mechanics and controlled release. *Advanced Materials*, 26, 2205.

[6] Drews, A. M., Cademartiri, L., Chemama, M. L., Brenner, M. P., Whitesides, G. M., & Bishop, K. J. M. (2012). *Physical Review E*, 86, 36314.

[7] Duncanson, W. J., Lin, T., Abate, A. R., Seiffert, S., Shah, R. K., & Weitz, D. A. (2012). Microfluidic synthesis of advanced microparticles for encapsulation and controlled release. *Lab on a Chip*, 12, 2135.

[8] Fialkov, A. (1997). Investigations on ions in flames. *Progress in energy and combustion science*, 23, 399.

[9] Floury, J., Desrumaux, A., & Lardières, J. (2000). Effect of high-pressure homogenization on droplet size distributions and rheological properties of model oil-in-water emulsions. *Innovative Food Science and Emerging Technologies*, 1, 127.

[10] Gilbert, W. (1600). De Magnete, Magneticisque Corporibus, et de Magno Magnete Tellure.

[11] Guenault, E. M. & Wheeler, R. V. (1931). *J. chem. Soc.*, 134, 195.

[12] Guo, M. T., Rotem, A., Heyman, J. A., & Weitz, D. A. (2012). Droplet microfluidics for high-throughput biological assays. *Lab on a Chip*, 12, 2146.

[13] Haller, K. K., Poulikakos, D., Ventikos, Y., & Monkewitz, P. (2003). Shock wave formation in droplet impact on a rigid surface. *J. Fluid. Mech.*, 490, 1.

[14] Keck, C. M. & Muller, R. H. (2006). Drug nanocrystals of poorly soluble drugs produced by high pressure homogenisation. *European Journal of Pharmaceutics and Biopharmaceutics*, 62, 3.

[15] Kolinski, J. M., Rubinstein, S. M., Mandre, S., Brenner, M. P., Weitz, D. A., & Mahadevan, L. (2012). Skating on a film of air: drops impacting on a surface. *Phys. Rev. Lett.*, 108, 074503.

[16] Law, C. K. (1990). *Combustion Physics*, (pp. 165). Cambridge University Press.

[17] Lawton, J. & Weinberg, F. J. (1964). *Proc. Roy. Soc. A*, 277, 468.

[18] Lawton, J. & Weinberg, F. J. (1969). *Electrical Aspects of Combustion*. Oxford Clarendon Press.

[19] Lesser, M. B. (1981). Analytic solutions of liquid-drop impact problems. *Proc. R. Soc. Lond. A*, 377, 289.

[20] Mandre, S. & Brenner, M. P. (2012). The mechanism of a splash on a dry solid surface. *J. Fluid Mech.*, 690, 148.

[21] Mani, M., Mandre, S., & Brenner, M. P. (2010). Events before droplet splashing on a solid surface. *J. Fluid Mech.*, 647, 163.

[22] Mulligan, M. K. & Rothstein, J. P. (2012). Scale-up and control of droplet production in coupled microfluidic flow-focusing geometries. *Microfluidics and Nanofluidics*, 13, 65.

[23] Palmer, H. J. & Beer, J. M. (1974). *Combustion Technology, Some Modern Developments*. Academic Press Inc.

[24] Rayleigh, J. W. S. (1878). On the instability of jets. *Proceedings of the London Mathematical Society*, s1-10, 4.

[25] Rein, M. (1993). Phenomena of liquid drop impact on solid and liquid surfaces. *Fluid Dyn. Res.*, 12, 6193.

[26] Romanowsky, M. B., Abate, A. R., Rotem, A., Holtze, C., & Weitz, D. A. (2012). High throughput production of single core double emulsions in a parallelized microfluidic device. *Lab on a Chip*, 12, 802.

[27] Spyropoulos, F., Lloyd, D. M., Hancocks, R. D., & Pawlik, A. K. (2013). Advances in membrane emulsification. part a: recent developments in processing aspects and microstructural design approaches. *Journal of the Science of Food and Agriculture*, 94, 613.

[28] Teh, S. Y., Lin, R., Hung, L. H., & Lee, A. P. (2008). Droplet microfluidics. *Lab on a Chip*, 8, 198.

[29] Umbanhowar, P. B., Prasad, V., & Weitz, D. A. (2000). Monodisperse emulsion generation via drop break off in a coflowing stream. *Langmuir*, 16, 347.

[30] Utada, A. S., Chu, L. Y., Fernandez-Nieves, A., Link, D. R., Holtze, C., & Weitz, D. A. (2007). Dripping, jetting, drops, and wetting: The magic of microfluidics. *MRS Bulletin*, 32, 702.

[31] Vladisavljevic, G. T., Kobayashi, I., & Nakajima, M. (2012). Production of uniform droplets using membrane, microchannel and microfluidic emulsification devices. *Microfluidics and Nanofluidics*, 13, 151.

[32] von Smoluchowsky, M. (1906). Zur kinetischen Theorie der Brownschen Molekularbewegung und der Suspensionen. *Annalen der Physik*, 326, 756.

[33] Williams, F. A. (1994). *Combustion Theory*, chapter Appendix E2, On Diffusion. Westview Press.

[34] Worthington, A. M. (1876). On the forms assumed by drops of liquids falling vertically on a horizontal plate. *Proc. R Soc. Lond. A*, 25, 261.

[35] Xia, Y. N. & Whitesides, G. M. (1998). Soft lithography. *Angewandte Chemie International Edition*, 37, 551.

[36] Xu, L., Zhang, W. W., & Nagel, S. R. (2005). Drop splashing on a dry smooth surface. *Phys. Rev. Lett.*, 94, 184505.

[37] Yarin, A. L. (2006). Drop impact dynamics: Splashing, spreading, receding, bouncing... *Annu. Rev. Fluid Mech*, 38, 159.